# Computer simulations of a two-dimensional system with competing interactions

Antitsa D. Stoycheva and Sherwin J. Singer

*Department of Chemistry, Ohio State University, 100 W. 18th Avenue, Columbus, Ohio 43210*
(Received 23 July 2001; published 19 February 2002)

The results and methodology of large scale computer simulations of the two-dimensional dipolar Ising model with long-range interactions are reported. Systems as large as 117 649 particles were studied to elucidate the elementary excitations and phase diagram of two-dimensional systems, such as Langmuir monolayers, thin garnet films, and adsorbed films on solid surfaces, which spontaneously form patterns of stripes, bubbles, and intermediately shaped domains. The challenging numerical investigations of large scale systems with long-range interactions at low temperatures were made possible by combining the fast multipole method and a non-Metropolis Monte Carlo sampling technique. Our simulations provide evidence that, at sufficiently high ratios of the repulsive to the attractive coupling constant for the model, twofold stripe order in the systems of interest is lost through a defect-mediated mechanism. Heat capacity data and the excitations observed in our simulations as the system disorders indicate that it is most likely an instance of a Kosterlitz-Thouless phase transition. The results from simulations with and without external field are in excellent agreement with the predictions of an analytic scaling theory [A. D. Stoycheva and S. J. Singer, Phys. Rev. E **64**, 016118 (2001)], confirming the phase diagram furnished by the analytic model. The scaling theory suggests that, under certain conditions, defect-mediated stripe melting may be supplanted by Ising like disordering within stripes for small repulsion strength. A qualitative discussion of a model that supports both disordering mechanisms is presented.

## I. INTRODUCTION

Competing attractive and repulsive interactions generate spontaneous spatial modulations in a diverse collection of two- and three-dimensional systems in nature [1]. This paper reports an implementation of large scale computer simulations of a fundamental model for modulated materials, such as Langmuir monolayers, thin magnetic films, and adsorbed monolayers on solid surfaces. Patterns of stripes, bubbles, and intermediately shaped domains arise in these systems due to the competition between attractions and longer-range repulsions. Our numerical investigations of systems with long-range interactions of sizes up to $O(10^5)$ particles provide insight into the critical excitations and phase diagram of spontaneously modulated phases. They elucidate how these properties evolve as a function of the relative repulsion strength, defined as the ratio of the repulsive to the attractive interaction constant. This work augments an earlier paper on large scale simulations [2] and tests an analytic scaling theory [3] derived for the dipolar Ising ferromagnet and its lattice gas equivalent.

Spontaneous spatial modulations were first observed in magnetic and dielectric systems [4–9]. Experimental studies of thin magnetic films [5,9] and fluids with magnetic or electric polarization [7] have revealed the occurrence of modulated phases—patterns of stripes, bubbles, or intermediate morphologies. In three dimensions, the patterns may be extensions of the two-dimensional (2D) morphologies along a third dimension, such as lamelli or cylinders, or true three-dimensional modulations. It has been demonstrated that "stripe" to "bubble" phase transitions in magnetic films may be induced by varying an applied external field $H$ [5,9]. Stripe to bubble transitions occur when the width of the minority stripes falls below a certain threshold [5]. These transformations appear to be reversible, although some hysteresis

exists [5]. With few exceptions [10–14], the experimentally observed morphologies have been discussed in the zero-temperature limit, treating only perfectly straight stripes [4–9]. The experimentally observed domain structures, when sufficiently regular, can be quantitatively understood in terms of the already mentioned balance between short-ranged attractions and long-ranged repulsions. The attractions cause additional wall energy at domain borders, and the repulsions arise among magnetic or electric dipoles. The interplay of these effects determines the preferred modulation corresponding to a free energy minimum.

In the last couple of decades, the newly developed techniques of fluorescence and video microscopy have enabled the visualization and analysis of patterns resulting from phase transitions in thin lipid films at the air/water interface [15–19], as summarized in recent reviews [1,19,20]. These studies have shown that domain structures in surfactant monolayers are amazingly similar in appearance to modulations in ferromagnetic fluids and thin films [10]. The domain shapes have been demonstrated to be once again due to a balance between short-ranged attractive interactions, such as the van der Waals attractions between hydrocarbon chains [21] and long-ranged dipolar repulsions, arising from the interactions between dipolar phospholipid head groups or effective dipoles formed by the charged heads of the phospholipids and subphase counterions [17,19,18]. Pressure-[16,21,22] and temperature-induced [17] phase transitions in thin organic films appear to be reversible, although some hysteresis is present [17].

Recent experimental studies of adsorbed monolayers on surfaces [23–26] have provided evidence of 2D arrays of stripes [23,25,26], bubbles [24], and intermediate "labyrinth" structures [24] formed by the adsorbed atoms, analogous in appearance to the ones seen in thin ferromagnetic films and Langmuir monolayers. The spontaneous modula-

tion phenomena in adsorbed monolayers have been modeled using zero-temperature (with respect to domain shape fluctuations) elastic theory [27–29]. The similar effect of elastic and electrostatic interactions resulting in analogous phase modulations in 2D has been pointed out in Ref. [14] and summarized in Ref. [30]. As a consequence, a single model incorporating the interplay of short-ranged attractive and long-ranged repulsive interactions, regardless of their origin, may be applied to study all of the above-mentioned systems. Curvature instabilities in biological membranes have also been explained using the same theoretical model [31].

The reason for the apparently universal domain morphologies in two dimensions and the applicability of a single model is that the forces governing self-organization in the systems of interest act on a larger than molecular length scale. The nature of the short-ranged attractive forces varies between systems. The long-ranged repulsions in experimental systems studied to date are due to actual or effective dipoles and decay with distance as $R^{-3}$. Magnetostatic spin interactions govern the dipolar repulsion between domains in thin ferromagnetic films [4–9]. Surface polarization is the source of the repulsion in Langmuir monolayers [16–21,32]. Either surface polarization or accumulation of elastic energy from lattice mismatch cause actual or effective dipolar repulsion within adsorbed monolayers on solid substrates [30,33,34].

A simple Hamiltonian captures the essential features needed to describe the behavior of the above mentioned systems (notation appropriate for spin systems will be used in this paper),

$$-\mathcal{H}/k_B T = J \sum_{\langle R,R' \rangle} s_R s_{R'} - \frac{A}{2} \sum_{R,R'}{}' \frac{s_R s_{R'}}{|R-R'|^3} + h \sum_R s_R,$$

(1)

where $s_R$ and $s_{R'}$ are uniaxial spin variables for spins at sites $R$ and $R'$, $J$ is an attractive coupling constant ($J>0$), $A$ is a repulsive coupling constant ($A>0$), and $h$ is an external field. The first term in the above equation captures the short-range nearest-neighbor interactions of a system of Ising spins, the second term mimics the long-range repulsions. The prime indicates that $R=R'$ is excluded from the sum. The third term takes into account the influence of an external magnetic field. The Hamiltonian of Eq. (1) turns into one for a dipolar lattice gas after the variable substitution $s_R = 2n_R - 1$, where $n_R = 0$ or 1 is the lattice gas occupation variable. We also introduce the temperature-independent parameter $\eta \equiv A/J$, the ratio of the repulsive coupling constant $A$ over the attractive coupling constant $J$ in Eq. (1), which measures the relative repulsion strength in the system. Throughout this paper, distances are measured in units of the nearest neighbor distance of the lattice, so quantities like $A$ are dimensionless.

The model of Eq. (1) has sparked a lengthy discussion concerning its phase diagram and the types of elementary excitations leading to phase transitions. Both order parameter fluctuations and topological defects, such as dislocations and disclinations, have been considered as factors leading to the destruction of orientational order in modulated phases. A self-consistent field theory by Brazovskiĭ [35], valid for small order parameter values, for a continuum spin model with long range repulsions indicated a first-order phase transition between isotropic and nonuniform states in the system. Toner and Nelson [36] studied the effects of both phonon-like fluctuations and Kosterlitz-Thouless (KT)-type unbinding of topological defects on 2D layered materials. They pointed out that dislocations, present with a Boltzmann-distributed density at any finite temperature, are responsible for the loss of translational order and the algebraic decay of orientational correlations in the low temperature phase. Unbinding of dislocations into pairs of disclinations at the KT phase transition destroys orientational order, leading to exponential decay of orientational correlations. Toner and Nelson predicted the phase diagram applicable to 2D layered materials in the presence of topological defect unbinding. Garel and Doniach [37] investigated the phase diagram of a uniaxial ferromagnet using a Ginzburg-Landau mean-field approach, but also discussed the effects of topological defect unbinding on the degree of 2D order of the modulated phases. They were unable to determine which mechanism was responsible for the loss of twofold order. Andelman *et al.* [32] analyzed insoluble Langmuir monolayers with a Ginzburg-Landau expansion. Within a mean-field approximation they obtained results that are in qualitative agreement with the corresponding analysis of the ferromagnetic system presented in Ref. [37]. Our recent work [2,3] has shed new light on these issues and has furnished a theoretical explanation for previously puzzling experimental observations, such as pressure-induced stripe melting in Langmuir monolayers [22].

In this paper, we investigate the mechanisms leading to the loss of twofold order of the stripe phase in Langmuir monolayers, thin magnetic films, and adsorbed monolayers, a process we refer to as "stripe melting." We present evidence, based on our computer simulations, for the role of dislocations and disclinations in the 2D systems of interest. Our numerical results for the heat capacity show smooth behavior of $C_v$ near the stripe melting temperature $T_m$, as predicted by KT theory. The computer simulation results are in excellent agreement with an analytic scaling theory for two-dimensional systems with competing interactions presented elsewhere [3]. We compare numerical data to the analytic theory phase diagram [3]. Other possible experimental tests for our theoretical findings are suggested.

This paper is organized as follows: The computer simulation techniques we used are introduced in Sec. II. In Sec. III, we discuss our numerical results. The implications of our work are considered in Sec. IV. The statistical analysis of our simulation data and details concerning the Monte Carlo algorithm are given in the Appendixes.

## II. SIMULATION TECHNIQUES

Previous simulations for the dipolar Ising model on triangular [11,13] and square [38,39] lattices have confirmed that the Hamiltonian of Eq. (1) supports the experimentally observed morphologies—stripes, bubbles, and elongated intermediate domains—in the 2D systems of interest.

Several essential problems have to be addressed to simulate the model of Eq. (1).

(1) Since the dipolar interactions are long ranged and give rise to long-wavelength modulated structures, simulation systems must be large enough to capture this behavior. This requirement can place insurmountable limitations on computer codes relying on explicitly summing the interactions over all spin pairs. [Recall that the Hamiltonian in Eq. (1) includes repulsive interactions between all spin pairs, not just nearest neighbors.] For direct sum approaches, each attempted spin update requires a number of floating point operations, which grow linearly with system size. Previously published results for the dipolar lattice gas on a triangular lattice are available for a periodically replicated unit cell of as many as 15 776 [11–13], but more typically about 3000 spins [11,13]. For the Ising model on a square lattice, the largest size of the periodic replicas was 4096 particles [38,39]. In this work, we report simulations of systems as large as 117 649 spins.

(2) The systems described by Eq. (1) contain large domain structures whose movement is slow in numerical simulations and which require long equilibration times. At the low temperatures in consideration, much lower than the critical temperature of the Ising model without long-range repulsions, Metropolis Monte Carlo (MC) algorithms perform inefficiently.

In order to accommodate the above-mentioned requirements, we have employed the fast multipole method (FMM) [40] and a non-Metropolis sampling technique [41,42].

## A. The fast multipole method

We have implemented the FMM introduced by Greengard and Rokhlin [40]. A recent review summarizes its features in three dimensions and compares it to Ewald sum and particle mesh-based approaches [43]. The FMM has previously been used in continuous-model simulations in two [40] and three [44] dimensions. We have devised a scheme that applies to simulations on a lattice. A considerable advantage of our FMM implementation, discussed in detail in the following sections, is that transferring quantities needed to calculate the interaction potential between levels in the FMM hierarchy involves a set of precomputed matrices that do not depend on the level.

Using the FMM circumvents calculating the long-ranged $R^{-3}$ depolarizing interaction potential via CPU-intensive direct summation methods, as was done in previous work [11–13]. The FMM reduces the work required to calculate the total energy of a system of $N$ particles from $O(N^2)$ to $O(N)$, and the amount of work per MC target update from $O(N)$ to $O(\ln N)$ compared to direct-sum methods [43]. For concreteness, we illustrate the implementation of the FMM on a 2D triangular lattice. The FMM can be applied to other lattice geometries and systems in other dimensions in the manner we describe with minor modifications.

The FMM requires a recursive division of the simulation cell into a hierarchy of levels. We designate the simulation cell itself as level $l=0$, and the lattice spins as $l=l_{max}$. For the case of a triangular lattice in 2D, we choose a hexagon as
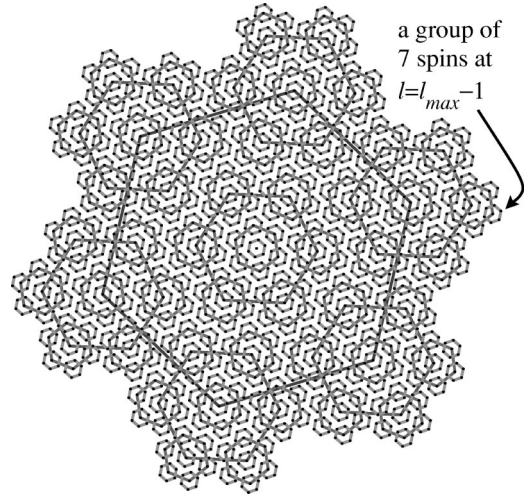


FIG. 1. FMM hierarchy on a two-dimensional triangular lattice.

the building block for the hierarchy into which we partition the system. At level $l=l_{max}-1$, the spins are grouped into hexagons consisting of a spin and its six nearest neighbors on a triangular lattice. The spins are represented by black dots in Fig. 1, and a hexagon containing seven spins is indicated. Upon going from level $l_{max}-1$ to $l_{max}-2$, seven hexagons, each containing seven spins, are grouped so that their centers form the vertices and center of a larger hexagon. Thus, at $l_{max}-2$, the hexagonal spin groups contain 49 spins. Subsequently, seven groups of 49 spins are brought together to form a hexagon containing 343 spins at level $l_{max}-3$ and so on until $l=0$ is reached. The system in Fig. 1 has $l_{max}=4$, corresponding to a total of $7^4$ or 2401 spins. This particular choice of a recursive scheme is the reason why the sizes of the systems we simulated have been expressed in powers of the integer 7 throughout the paper. A very convenient feature of the recursively generated hierarchy of hexagons is that the constituent elements at each level $l$, blocks of $7^{l_{max}-l}$ spins, are always arranged on a triangular lattice whose basis vectors are denoted by $\mathbf{b}_1(l)$ and $\mathbf{b}_2(l)$. The basis vectors at the level of the individual spins $l=l_{max}$, $\mathbf{b}_1(l_{max})$ and $\mathbf{b}_2(l_{max})$ (Fig. 2), connect the center of a group of seven spins with the nearest neighbor at the "three o'clock" lattice location and to the "one o'clock" nearest neighbor location, respectively. In Cartesian coordinates, they are given by
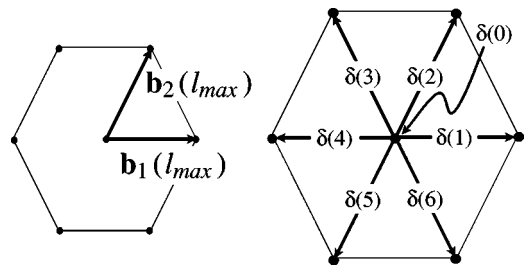


FIG. 2. Basis vectors $\mathbf{b}_i(l_{max})$ at level $l_{max}$ and displacements $\delta_i(j_l)$ from the center of a group of seven spins.

$$\mathbf{b}_1(l_{max}) = \begin{pmatrix} 1 \\ 0 \end{pmatrix}, \quad \mathbf{b}_2(l_{max}) = \begin{pmatrix} \frac{1}{2} \\ \frac{\sqrt{3}}{2} \end{pmatrix}. \qquad (2)$$

Basis vectors for subsequent levels of the FMM hierarchical structure are related by the following linear transformation

$$\begin{pmatrix} \mathbf{b}_1(l) \\ \mathbf{b}_2(l) \end{pmatrix} = \frac{1}{7} \begin{pmatrix} 3 & -1 \\ 1 & 2 \end{pmatrix} \begin{pmatrix} \mathbf{b}_1(l-1) \\ \mathbf{b}_2(l-1) \end{pmatrix} \equiv \mathbf{A} \begin{pmatrix} \mathbf{b}_1(l-1) \\ \mathbf{b}_2(l-1) \end{pmatrix}. \quad (3)$$

Note that the matrix $\mathbf{A}$ remains the same, regardless of the values of $l$ and $l-1$. From the above relations,

$$|\mathbf{b}_i(l-1)| = \sqrt{7}|\mathbf{b}_i(l)|. \qquad (4)$$

The primary simulation cell and its periodic replicas are at level $l=0$ in the FMM hierarchy, and the basis vectors corresponding to $l=0$ are $\mathbf{b}_i(0)$. The locations of periodic replica centers, relative to the center of the primary simulation cell that is taken as the origin of our coordinate system, may be expressed as $\mathbf{R}=q_i\mathbf{b}_i(0)$, where $q_i$ are integers, and the convention for summation of repeated indices is in force.

The location of any point $\mathbf{R}$ at level $l$ within the primary simulation cell can be uniquely decomposed as

$$\mathbf{R}(j_1, \ldots, j_l) = \sum_{l'=1}^{l} \delta_i(j_{l'})\mathbf{b}_i(l') \quad (0 \le j_{l'} \le 6). \quad (5)$$

$\delta_i(j_l)$ are defined to indicate the displacement (if any) from the center within a group of seven spins, as illustrated in Fig. 2, and have the following values:

$$[\delta_1(0), \delta_2(0)] = (0,0), \qquad (6)$$

$$[\delta_1(1), \delta_2(1)] = (1,0),$$

$$[\delta_1(2), \delta_2(2)] = (0,1),$$

$$[\delta_1(3), \delta_2(3)] = (-1,1),$$

$$[\delta_1(4), \delta_2(4)] = (-1,0),$$

$$[\delta_1(5), \delta_2(5)] = (0,-1),$$

$$[\delta_1(6), \delta_2(6)] = (1,-1).$$

Due to the hierarchical arrangement of hexagons in the system, $\delta_i(j_l)$ also give the location of a group of $7^{l_{max}-l}$ spins at level $l$ in the hierarchy relative to a hexagon center at level $l-1$. Therefore, specifying the $j_l$ index for levels 1 through $l$ is sufficient to locate a target group at level $l$, and its "address" is a number in base 7. In our simulations, groups of seven spins at $l_{max}-1$ were targeted for Monte Carlo updates. The address of the target indicated by the arrow in Fig. 1 is {166}.

Using the above-introduced notation, we develop an expression for the long-range $R^{-3}$ repulsive interaction energy in the system,

$$V = \frac{1}{2} \sideset{}{'}\sum_{\mathbf{R},\mathbf{R}',n_1,n_2} s_{\mathbf{R}}s_{\mathbf{R}'}|\mathbf{R}-\mathbf{R}'+n_i\mathbf{b}_i(0)|^{-3}, \qquad (7)$$

which we calculate using the FMM. The $n_i$ index the periodic replicas of the primary cell (for which $n_1=n_2=0$), and $\mathbf{R}$ and $\mathbf{R}'$ are the positions of spins $s_{\mathbf{R}}$ and $s_{\mathbf{R}'}$, respectively. The prime on the sums indicates that self-interactions are excluded. Repeated indices are summed. In a direct-sum approach, $\Sigma'_{\mathbf{R},\mathbf{R}',n_1,n_2}|\mathbf{R}-\mathbf{R}'+n_i\mathbf{b}_i(0)|^{-3}$ would be precomputed and stored in an array labeled by $\mathbf{R}$ and $\mathbf{R}'$. The FMM calls for a rearrangement of the sum in Eq. (7) into intragroup terms for target groups $G$ (chosen in our case to be hexagonal groups of seven spins) and intergroup interactions

$$V = \frac{1}{2} \sum_G \sideset{}{'}\sum_{\mathbf{R},\mathbf{R}'\in G} s_{\mathbf{R}}s_{\mathbf{R}'}|\mathbf{R}-\mathbf{R}'|^{-3} + \frac{1}{2} \sum_G \sum_{\mathbf{R}\in G} s_{\mathbf{R}}\Phi_G(\mathbf{R}).$$

The field $\Phi_G(\mathbf{R})$ acts as an effective magnetic field on each of the spins within a target group $G$. It is given by

$$\Phi_G(\mathbf{R}) = \sum_{\mathbf{n}} \sum_{G'(\neq G \text{ if } \mathbf{n}=0)} \sum_{\mathbf{R}'\in G'} s_{\mathbf{R}'}|\mathbf{R}-\mathbf{R}'+n_i\mathbf{b}_i(0)|^{-3},$$

$$\mathbf{R}\in G. \qquad (8)$$

Since both $G$ and $G'$ may belong to the primary simulation cell ($\mathbf{n}=\mathbf{0}$), self-interactions must be excluded ($G'\neq G$, if $\mathbf{n}=\mathbf{0}$). When $G'$ lies outside the primary cell, it is either a periodic replica of $G$ itself interacting with $G$ ($G'=G$, $\mathbf{n}\neq\mathbf{0}$), or another periodically replicated group interacting with $G$ ($G'\neq G$, $\mathbf{n}\neq\mathbf{0}$). One key advantage of the FMM is that the initial calculation of $\Phi_G(\mathbf{R})$ for *all* groups $G$, i.e., the second term in Eq. (8), requires only $O(N)$ operations.

At the beginning of a simulation, the repulsive interaction field of the entire system is calculated in what is called an "upward pass." To achieve that, a multipole expansion is initially computed for all groups $G$ and the hierarchy of larger groups. Following each MC update, the upward pass is required to generate new multipole moments only for groups at each level whose spin configuration has changed. Second, the collection of precomputed multipole moments is used to calculate an effective potential for target spin groups in what is called a "downward pass." At the start of program execution, a complete downward pass for all spin groups is performed to calculate the total energy of the initial configuration. All steps involved require $O(N)$ operations, compared to $O(N^2)$ operations in a direct sum calculation.

Monte Carlo updates of a target group $G$ consist of three separate steps. First, a calculation of the effective field $\Phi_G(\mathbf{R})$ at that group, based on precomputed multipole moments, is required. This corresponds to a partial downward pass. Subsequently, the energy change associated with the actual spin flip is evaluated. Finally, an update of multipole moments, a partial upward pass, follows. There is a fixed operation count at each level of the partial upward and downward passes. Since the number of levels is $O(\ln N)$,
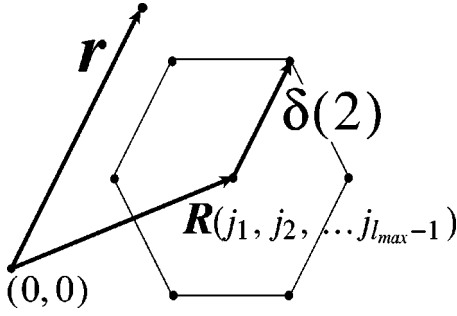
FIG. 3. Contribution to the effective field $\Phi(\mathbf{r})$ at a test point $\mathbf{r}$ arising from a group of seven spins centered at $\mathbf{R}(j_1, j_2, \ldots j_{l_{max}-1})$.

each update of a target group requires $O(\ln N)$ operations, and an entire MC pass requires $O(N \ln N)$ operations.

### 1. Multipole moment functions and the upward pass

We use a multipole expansion to derive a form of $\Phi_G(\mathbf{R})$, which is particularly useful for efficient calculation of the interaction potential during computer simulations. As an example, consider the effective field $\Phi(\mathbf{r})$ at a test point $\mathbf{r}$ arising from a group of seven spins centered at $\mathbf{R}(j_1, \ldots, j_{l_{max}-1})$ (Fig. 3),

$$
\Phi(\mathbf{r})
$$

$$
= \sum_{j_{l_{max}}=0}^{6} \frac{s_{[\mathbf{R}(j_1, \ldots, j_{l_{max}-1}) + \delta_i(j_{l_{max}})\mathbf{b}_i(l_{max})]}}{|\mathbf{r} - [\mathbf{R}(j_1, \ldots, j_{l_{max}-1}) + \delta_i(j_{l_{max}})\mathbf{b}_i(l_{max})]|^3}
$$

$$
= \sum_{k_1, k_2=0}^{\infty} \mu[k_1 k_2 | \mathbf{R}(j_1, \ldots, j_{l_{max}-1})]
$$

$$
\times \theta[k_1 k_2 | \mathbf{r} - \mathbf{R}(j_1, \ldots, j_{l_{max}-1})]. \tag{9}
$$

In the above equation, $\theta(k_1 k_2 | \mathbf{r})$ are multipole functions defined as

$$
\theta(k_1 k_2 | \mathbf{r}) \equiv \frac{1}{k_1! k_2!} \frac{\partial^{k_1 + k_2}}{\partial r_1^{k_1} \partial r_2^{k_2}} |\mathbf{r}|^{-3}, \tag{10}
$$

where $r_i$ are the components of $\mathbf{r}$, so that $\mathbf{r} = r_i \mathbf{b}_i$. For a triangular lattice in 2D,

$$
|\mathbf{r}|^{-3} = (r_1^2 + r_2^2 + r_1 r_2)^{-3/2}. \tag{11}
$$

Note that the multipole decomposition has general validity and does not depend on the dimension of the vector $\mathbf{r}$, or the type of interaction. For an $n$-dimensional vector $\mathbf{r}$ and an interaction that goes as $\mathbf{r}^p$, the multipole expansion has the form

$$
\theta(k_1 k_2 \cdots k_n | \mathbf{r}) \equiv \frac{1}{k_1! k_2! \cdots k_n!} \frac{\partial^{k_1 + k_2 + \cdots k_n}}{\partial r_1^{k_1} \partial r_2^{k_2} \cdots \partial r_n^{k_n}} |\mathbf{r}|^p. \tag{12}
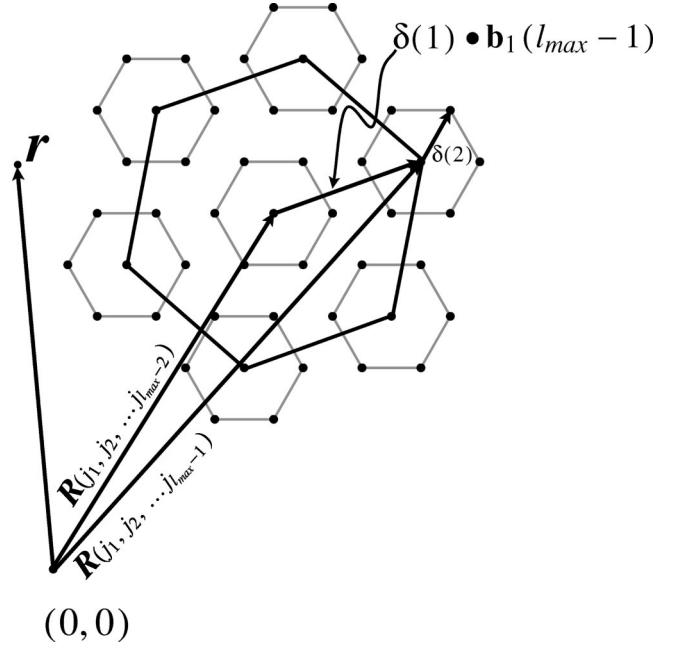$$



FIG. 4. Coordinate system for shifting the interaction potential $\Phi(\mathbf{r})$ experienced by a particle at position $\mathbf{r}$ from an interaction center at level $l_{max}-1$ to an interaction center at level $l_{max}-2$.

$\mu[k_1 k_2 | \mathbf{R}(j_1, \ldots, j_{l_{max}-1})]$ are multipole moment coefficients appropriate for groups of seven spins at level $l_{max} - 1$. They contain the spin configuration dependence of the multipole expansion. If any of the seven spin variables $s_{[\mathbf{R}(j_1, \ldots, j_{l_{max}-1}) + \delta_i(j_{l_{max}})\mathbf{b}_i(l_{max})]}$ in Eq. (9) changed its value, the effect on the multipole moment expansion in the system would be reflected by a different $\mu[k_1 k_2 | \mathbf{R}(j_1, \ldots, j_{l_{max}-1})]$ coefficient. The multipole functions $\theta(k_1 k_2 | \mathbf{r})$ remain the same upon a change of the spin configuration.

Following the concept of the upward pass, consider going one step higher in the hierarchy of the system. This corresponds to shifting $\Phi(\mathbf{r})$ to a new expansion center $\mathbf{R}(j_1, \ldots, j_{l_{max}-2})$ at level $l_{max} - 2$, illustrated in Fig. 4. The new expression for the shifted multipole coefficients $\mu$ is

$$
\mu[k_1 k_2 | \mathbf{R}(j_1, \ldots, j_{l_{max}-2})]
$$

$$
= \sum_{j_{l_{max}-1}=0}^{6} \sum_{k_1', k_2'} D_{j_{l_{max}-1}}(k_1 k_2 | k_1' k_2')
$$

$$
\times \mu[k_1' k_2' | \mathbf{R}(j_1, \ldots, j_{l_{max}-1})]. \tag{13}
$$

The sum over $j_{l_{max}-1}$ indicates that there are seven groups of seven spins at level $l_{max} - 1$ that contribute to a single group at level $l_{max} - 2$. The $D_j(k_1 k_2 | k_1' k_2')$ are elements of a matrix that is the same for a shift from any level $l$ to level $l-1$, and are calculated by straightforward, but tedious, series expansion of the multipole functions. Therefore, the above expression holds for all levels $l$,

$$\mu[k_1 k_2 | \mathbf{R}(j_1, \ldots, j_{l-1})]$$

$$= \sum_{j_l=0}^{6} \sum_{k_1', k_2'} D_{j_l}(k_1 k_2 | k_1' k_2') \mu[k_1' k_2' | \mathbf{R}(j_1, \ldots, j_l)].$$

$$(14)$$

Several points to note about the multipole moments in the system are the following. At the level of individual spins, $l = l_{max}$, the only contributing term has $k_1 = 0$ and $k_2 = 0$. The multipole moment coefficient is $\mu[00 | \mathbf{R}(j_1, \ldots, j_{l_{max}})]$ $= s_{\mathbf{R}(j_1, \ldots, j_{l_{max}})} |\mathbf{b}_i(l_{max})|^{3/2}$ for a triangular lattice, and we adopt the convention that $|\mathbf{b}_i(l_{max})| = 1$. Higher multipole moments emerge when spins are brought together in groups and the effective field is expanded about alternative reference points, as shown above. During this procedure, old multipole moments only give rise to new multipole moments of the same or higher order. We checked the convergence of the multipole expansion performing calculations with $k_1$ and $k_2$ as large as 20. It was established that results converged for a maximum power of 2 in the $k$ indices.

### 2. Downward pass

After an initial upward pass, the total repulsive potential field at level $l = 0$ and all sublevels is known. The downward pass calculates the interaction potential for a group of spins at a chosen level $l$. Depending on their proximity to the target, the other groups of spins in the system give rise to either "far field," or "interaction list" [40] contributions. Multipole expansions are used to calculate the far field, while contributions from members of the interaction list are computed explicitly. In our simulations, the interaction list for a group of $7^{l_{max}-l}$ spins at level $l$ includes its six nearest-neighbor groups, i.e., a total of $6(7^{l_{max}-l})$ spins. The interaction list of our targets for spin flips, groups of seven spins at level $l_{max} - 1$, includes the 42 spins that belong to the six nearest-neighbor hexagons of the target. Figure 4 illustrates a target for a MC update (central hexagon) and its six nearest neighbors containing the interaction list. All other spins in the system contribute to the interaction potential at the target through the far field.

The interaction field is brought from $l = 0$ to $l = l_{max} - 1$ through a series of linear transformations, referred to as "shift" and "rotate" operations. A shift operation consists of reexpressing the field from an expansion about an interaction center at level $l$ to an expansion about a center at level $l + 1$. The interaction center for a given level $l$ is defined as the midpoint of the central hexagon containing $7^{l_{max}-l}$ spins at that level. For instance, in Fig. 4, the shift brings the center of the interaction potential expansion from $\mathbf{R}(j_1, \ldots, j_{l_{max}-2})$ to $\mathbf{R}(j_1, \ldots, j_{l_{max}-1})$. The rotation that follows is the recalibration of the basis vectors $\mathbf{b}_i$ according to Eq. (3). The downward pass is summarized in the following steps: (1) Add far field contribution for $l = 0$, an Ewald summation of the repulsive field from a lattice of periodically replicated simulation cells; (2) Shift and rotate to interaction center at $l = 1$; (3) Divide $l = 0$ interaction list into $l = 1$ far field and $l = 1$ interaction list; (4) Add far field con-

tribution for $l = 1$; (5) Shift and rotate to interaction center at $l = 2$; (6) Divide $l = 1$ interaction list into $l = 2$ far field and $l = 2$ interaction list; $\ldots$, and so on until the far field and interaction list contributions at $l_{max-1}$ have been calculated.

In order to cast the above steps in mathematical terms, consider $\mathbf{\Phi}(\mathbf{r})$ arising at a test point $\mathbf{r}$ from a group of spins centered at $\mathbf{R}(j_1, \ldots, j_l)$ at level $l$. Let us first examine the far field. Using $t_i, i = 1, 2$ to stand for the components of the vector from the spin group at $\mathbf{R}(j_1, \ldots, j_l)$ to the field point $\mathbf{r}$,

$$\mathbf{r} - \mathbf{R}(j_1, \ldots, j_l) = t_i \mathbf{b}_i(l), \qquad (15)$$

where repeated indices are summed, we cast the interaction field $\mathbf{\Phi}(\mathbf{r})$ as a Taylor expansion,

$$\mathbf{\Phi}(\mathbf{r}) = \sum_{k_1, k_2=0}^{\infty} \gamma[k_1 k_2 | \mathbf{R}(j_1, \ldots, j_l)] t_1^{k_1} t_2^{k_2}. \qquad (16)$$

The series are constructed recursively: the expansion for an interaction center at $\mathbf{R}(j_1, \ldots, j_l)$ is obtained from the series about an interaction center at $\mathbf{R}(j_1, \ldots, j_{l-1})$, which in turn are obtained from the series at $\mathbf{R}(j_1, \ldots, j_{l-2})$, and so on. Switching interaction centers from level $l$ to $l + 1$, etc. corresponds to the already mentioned shift and rotate operations. The coefficients $\gamma[k_1 k_2 | \mathbf{R}(j_1, \ldots, j_{l+1})]$ at level $l + 1$ are related to $\gamma[k_1 k_2 | \mathbf{R}(j_1, \ldots, j_l)]$ at level $l$ as follows:

$$\gamma[k_1 k_2 | \mathbf{R}(j_1, \ldots, j_{l+1})]$$

$$= \sum_{k_1', k_2'} C_{j_{l+1}}(k_1 k_2 | k_1' k_2') \gamma[k_1' k_2' | \mathbf{R}(j_1, \ldots, j_l)]. \qquad (17)$$

$C_{j_{l+1}}(k_1 k_2 | k_1' k_2')$ are elements of a matrix independent of the level $l$ and evaluate to zero unless $k_1 + k_2 \leq k_1' + k_2'$.

The members of the far field and the interaction list change from level to level. Some groups of spins that were part of the interaction list at level $l$ are treated as far field using the finer degree of detail at level $l + 1$. We describe a procedure for incorporating repulsive energy contributions arising from groups of spins that were part of the interaction list at level $l$ into the far field for level $l + 1$. We designate this "correction" to the far field at level $l + 1$ by $\Delta \mathbf{\Phi}_G(\mathbf{r})$. The multipole moment coefficients $\mu[k_1 k_2 | \mathbf{R}(j_1, \ldots, j_l)]$ at level $l$, which can be used to define $\Delta \mathbf{\Phi}_G(\mathbf{r})$ following Eq. (9), have already been calculated in an upward pass preceding the downward pass. They are related to a correction $\Delta \gamma[k_1 k_2 | \mathbf{R}(j_1, \ldots, j_l)]$ at level $l$ as follows:

$$\Delta \mathbf{\Phi}_G(\mathbf{r}) = \sum_{\mathbf{R}(j_1, \ldots, j_l)} \sum_{k_1, k_2} \mu[k_1 k_2 | \mathbf{R}(j_1, \ldots, j_l)]$$

$$\times \theta[k_1 k_2 | \mathbf{r} - \mathbf{R}(j_1, \ldots, j_l)]$$

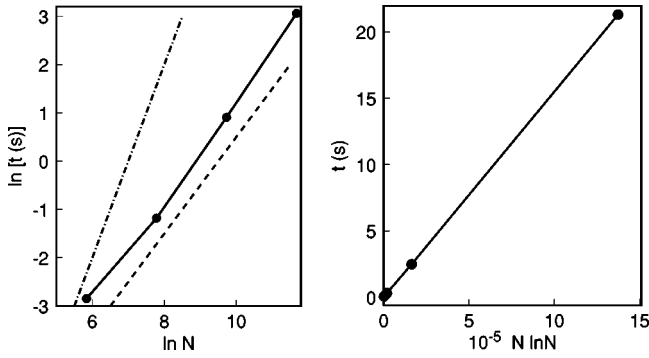$$= \sum_{k_1, k_2} \Delta \gamma[k_1 k_2 | \mathbf{R}(j_1, \ldots, j_l)] t_1^{k_1} t_2^{k_2}. \qquad (18)$$

FIG. 5. Scaling of CPU time ($t$) per Monte Carlo pass with total number of particles ($N$). The CPU times were measured on a Cray T90 computer for systems of sizes $7^p$, $p = 3,4,5,6$. Lines of slope equal to 1 (dashed line) and 2 (dot-dashed line) are shown in the log-log plot.

The coefficients $\Delta\gamma$ in the above equation are linear combinations of $\mu[k_1 k_2 | \mathbf{R}(j_1, \ldots, j_l)]$ which belong to the groups of spins forming the interaction list at level $l$,

$$\Delta\gamma[k_1 k_2 | \mathbf{R}(j_1, \ldots, j_l)]$$

$$= \sum_{\mathbf{R}'(j_1, \ldots, j_l)} \sum_{k_1', k_2'} M(k_1 k_2 | k_1' k_2')$$

$$\times \mu[k_1' k_2' | \mathbf{R}'(j_1, \ldots, j_l)]. \tag{19}$$

$M(k_1 k_2 | k_1' k_2')$ are elements of a matrix that does not depend on the level $l$. At level $l = 0$, the interaction list includes the nearest neighbor replicas of the primary simulation cell. Interactions with all other replicas contribute to the far field, and $\gamma(k_1 k_2 | \mathbf{0})$ is computed with the help of Ewald summation methods and stored.

The downward pass, associated with Monte Carlo updates of target spin groups, requires shifting and rotating $\Phi_G(\mathbf{r})$ to a new location $\mathbf{R}$ and the addition of a $\Delta\Phi_G(\mathbf{r})$ contribution from a fixed number of groups of spins. Since the number of levels $l$ in the simulated system is $O(\ln N)$, each update of a target group requires $O(N \ln N)$ operations, compared to $O(N^2)$ operations in a direct sum method. Figure 5 illustrates the scaling of CPU time with system size we achieved performing simulations on a Cray T90 System. The advantage of the FMM is obvious, especially at large system sizes.

### B. A cluster Monte Carlo algorithm

Simulations of the Ising model without long-range interactions at either low temperatures or near the critical point are characterized by numerical difficulties that have different origins. Both types of hindrances occur simultaneously in the pattern forming systems of interest and are addressed here. Phase transitions associated with domain morphologies are typically located at roughly 1/10 of the bare Ising model critical temperature, so spin flips needed to move domain boundaries can involve extremely small Boltzmann factors and, as a result, low acceptance rates. Complicating these "low temperature" difficulties is the fact that thermal fluctuations involve motion of domain structures whose length

scale can be quite large. Consequently, the "Monte Carlo time" required for their equilibration is long, and the same computational difficulties arise as in critical slowing down [45–47]. Cluster update techniques were developed in connection with the latter problem. They were introduced by Swendsen and Wang [48] and their efficiency was improved by Wolff [49]. The Wolff algorithm assures that every attempted cluster flip is accepted, leading to efficient sampling. The cluster update algorithms dramatically enhance the sampling of spin models, compared to Metropolis MC, regardless of their dimensionality and degrees of freedom [45–50]. However, no spin models with long-ranged interactions have been addressed to date. We present our implementation of cluster update techniques with the help of which we have overcome slow dynamics and have achieved high acceptance rates for the dipolar Ising model near criticality.

In the system we study, the Ising spins are organized on a triangular lattice into groups of seven to facilitate implementation of the FMM discussed in Sec. II A. The groups of seven spins are also used as the clusters for multispin updates. (Due to the long-ranged interactions, cluster selection according to the Wolff algorithm is not possible.) Each group thus has $2^7 = 128$ possible spin configurations, labeled by spin states $k = 0$ through $k = 127$. We arrange the cluster states in cyclical order, so that state $k = 127$ is followed by state $k = 0$. Traditional Metropolis MC methods only attempt a trial move to one of the possible 128 states per energy calculation, leading to low acceptance probabilities and extremely long equilibration times. To achieve better performance, we have implemented a variant of a cluster update algorithm proposed by Creutz [41,42], which in certain circumstances reduces to the Wolff algorithm [42], to treat a system with long-ranged interactions, such as the dipolar Ising model. The algorithm was originally introduced in the microcanonical ensemble [41] and it is convenient to explain it in that form before its trivial generalization to the canonical ensemble which we used.

A "demon" variable, capable of redistributing energy throughout the system, is introduced. A well-defined statistical system must have a ground state. We choose the demon ground state to have zero energy, so that $E_D \geq 0$. In the microcanonical version of the algorithm, the total energy of (system + demon) is conserved. The simulation progresses from an initial state where the demon has energy $E_D$, and the target cluster selected for update is in state $k_0$. The system initially possesses energy $E_0$. Moves to trial final states are attempted in some regular order. For our clusters of 7 spins, states are chosen by advancing through the 128 possible configurations (randomly in ascending or descending order), using the cyclical condition when state 0 or 127 is encountered. The first trial state for which energy conservation results in $E_D^{new} \geq 0$ is accepted. In the illustration of Fig. 6(a), $k - k_0 = 6$ is the first accessible cluster state. Here, the first accessible transition happens to result in a decrease of system energy. (In general, the system energy could either increase or decrease. Any trial state whose energy lies below the dashed line in Fig. 6(a) is energetically accessible.) After the move is taken in our example, the system energy drops and the demon energy rises—Fig. 6(b). A reverse move from
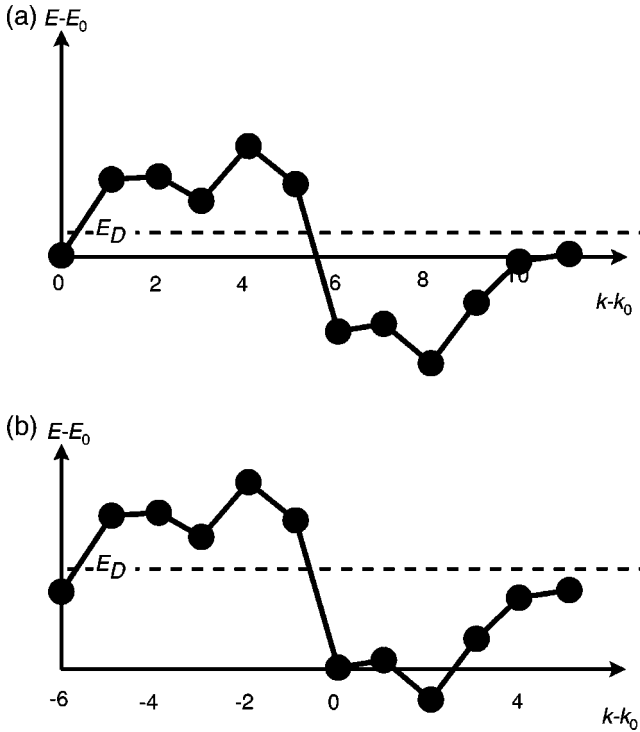
FIG. 6. Cluster updates in the microcanonical ensemble.

the final state depicted in Fig. 6(b) in the direction of decreasing index $k$ will bring the system right back to its initial state, because it is the first state encountered to which a transition is energetically allowed. The probabilities of attempting moves to states in ascending or descending order in the index $k$ are both 1/2. Therefore, the probabilities of the forward and reverse moves are equal and microcanonical detailed balance is satisfied.

We work in the canonical, rather than the microcanonical ensemble. This is achieved by drawing the demon's energy from a Boltzmann distribution $[P(E_D) \propto e^{-\beta E_D}]$ before each update. Physically, this corresponds to placing the system in contact with a heat bath whose relaxation time is much shorter than that of the system. A formal proof that this scheme enforces canonical detailed balance is given in Appendix A. Targets were picked at random. At each visit to a cluster, which entails a single calculation of the long-range dipolar field via the FMM, up to 127 new configurations

were considered for an acceptable energy-conserving move. This brings the acceptance rates to a typical value of $\sim 30\%$ for the dipolar Ising model, much higher than Metropolis MC at low temperature.

We achieved an additional speed-up by explicitly disabling attempts for spin updates for those randomly picked targets that were *not* situated along stripe interfaces. The probability of flipping a spin in the interior of a domain is proportional to $e^{-12J}$ times a correction for the long-range dipolar interaction. At typical $J$ and $A$ values used in this work, the probability of flipping interior spins is astronomically low and the system evolves exclusively by movement of the domain interfaces. Targets were classified as "interfacial" or "interior" to a stripe in the following manner.

If a target for an update was determined to have either "all up" or "all down" spins, the spin configuration of its six nearest-neighbor groups of seven spins was also checked. If all six nearest neighbors to the target had the same spin configuration as the target itself, then the target was determined to be interior to a stripe and no CPU time was spent on an attempt to update it, since the probability for an accepted move would be very small. If any of the nearest neighbors had a spin configuration different than that of the target, the target was considered for an update. By running the "full" version (i.e., without skipping any updates) of our computer code for a test case for each value of the relative repulsion strength $\eta \equiv A/J$ and system size, we checked that this feature did not alter the statistical sampling of targets. In general, this approach should be used with caution (and we did), especially for systems with low $\eta$ values whose stripe melting temperature lies highest among the systems we examined.

To test the cluster update algorithm, we calculated the average magnetization per spin $\langle m \rangle$ with no long-ranged repulsive interactions, so the numerical results could be compared with the exact solution for the Ising model [51]. (Of course, we did not skip "interior" spin updates in the absence of repulsive interactions and domains.) Under these circumstances, we recover the expected values of $\langle m \rangle = 0$ above the critical temperature and $\langle m \rangle = \pm 1$ at $T \ll T_c^{Ising}$. For temperatures between these two limits, we compared the results obtained with our variant of the Creutz algorithm to $\langle m \rangle$ from ordinary Metropolis MC and analytic values for the magnetization [52]. The data are presented in Table I.

TABLE I. Average magnetization per spin obtained from the Creutz algorithm, Metropolis MC, and analytic theory. For each temperature, the systems were equilibrated for 20 000 passes and simulation data were collected for 180 000 MC passes. Simulations were performed for systems of $7^4 = 2401$ spins for the Creutz algorithm and 2688 spins for the Metropolis algorithm. Acceptance rates are indicated in parentheses.

| $J$ | $\langle m \rangle_{Creutz}$ | $\langle m \rangle_{Metropolis}$ | $\langle m \rangle_{analytic}$ |
|---|---|---|---|
| 0.285 | $0.790 \pm 0.005$ (43.6%) | $0.788 \pm 0.003$ (16.1%) | 0.789 644 |
| 0.300 | $0.870 \pm 0.001$ (33.4%) | $0.8695 \pm 0.0004$ (11.4%) | 0.869 596 |
| 0.310 | $0.8975 \pm 0.0005$ (28.5%) | $0.8977 \pm 0.0004$ (9.4%) | 0.897 662 |
| 0.350 | $0.9525 \pm 0.0005$ (15.7%) | $0.9525 \pm 0.0001$ (4.6%) | 0.952 501 |
| 1.000 | $0.999\,986 \pm 0.000\,003$ (0.0057%) | $0.999\,987\,7 \pm 0.000\,000\,5$ (0.123%) | 0.999 988 |
| 2.500 | $1.0 \pm 2.4 \times 10^{-16}$ (0.00%) | $0.32 \pm 0.05$ (3.41%) | 1.000000 |

The analytic critical temperature for the bare Ising model on a triangular lattice corresponds to $J_c = 0.274\,653$ [52]. Simulations for either algorithm were started from random spin configurations.

For all temperatures presented in Table I, the average magnetization per spin obtained through the Creutz algorithm is in excellent agreement with the analytic results. The Creutz algorithm yields about three times higher acceptance rates compared to Metropolis MC at low temperatures, as shown in Table I. At extremely low temperatures, $J = 1.000$ and $J = 2.500$, both the Creutz and Metropolis algorithms show very low acceptance rates since virtually all the spins have the same orientation. Once the system approaches the Ising model ground state, departures from perfectly aligned spins are rare. However, even in this limit the Creutz algorithm is superior to Metropolis sampling. At $J = 2.500$, the Metropolis algorithm fails to equilibrate to a configuration whose magnetization has the expected value of 1.0 and instead reports $\langle m \rangle = 0.32 \pm 0.05$ for this temperature. At very low temperature, the system, starting from a random initial configuration, initially formed two large domains. Even after 400 000 Monte Carlo passes, the system was not able to approach the uniform ground state with Metroplis sampling. The relatively large acceptance rate for the Metropolis method is purely an artifact of the two-phase interface that this method could not relax. We emphasize that the acceptance rates in Table I are specific to simulations of the bare Ising model, and are much higher at the same temperature for a system of domains stabilized by long-ranged repulsions. In our numerical investigations of the dipolar Ising model, the lowest studied temperature was $J = 2.4$ (ordered stripe phase for $\eta = 0.43$) with corresponding acceptance rate of 28.4%.

## III. COMPUTER SIMULATION RESULTS

We report our results from very large scale computer simulations at finite temperatures for a 2D Ising ferromagnet described by Eq. (1). The inverse of the dimensionless attractive coupling constant $J$ is used as a measure of temperature: $T = 1/J$. Implementing a combination of the FMM and non-Metropolis MC sampling, the simulation of systems containing up to $7^6$ particles, roughly 40 times larger than was previously [11–13] attainable, has been made possible. Being able to handle very large systems allowed the study of a range of relative repulsion strengths $\eta$. For comparison, our previous investigations [11–13] were limited to $\eta = 0.43$, since system size increases faster than exponentially as $\eta$ is lowered [3]. In order to test our analytic theory predictions for the phase behavior of the dipolar ferromagnet [3] and the capabilities of the combined FMM and non-Metropolis sampling techniques, we have investigated systems with relative repulsion strengths varying from $\eta = 0.43$ to $\eta = 0.27$ in zero and finite external fields $h$.

### A. Simulations in zero external field

Systems with $\eta$ varying from 0.27 to 0.43 were investigated. For each $\eta$, a range of temperatures corresponding to
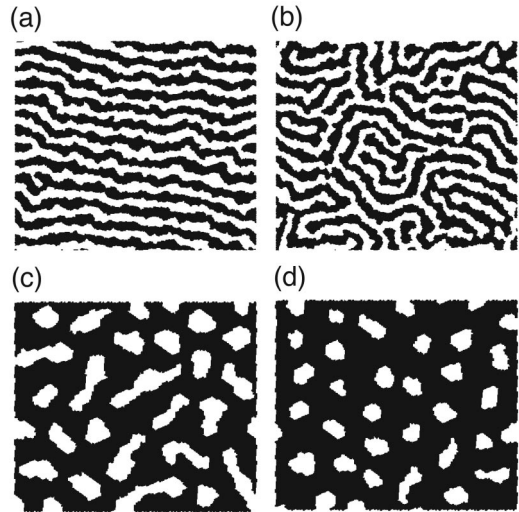


FIG. 7. Typical snapshots from computer simulations: (a) ordered stripe phase, (b) isotropic phase: "melted" stripes, (c) isotropic phase: elongated bubbles, (d) isotropic phase: bubble domains.

the ordered and disordered phases [53] was studied. The vicinity of $T_m$, the temperature at which twofold order was lost in the system, was determined for all $\eta$. Figures 7(a) and 7(b) show typical configurations from the ordered and "melted" stripe phases for a system of $7^6$ spins at $\eta = 0.27$, the lowest value accessible to our simulations, corresponding to the largest stripe period and the largest number of particles.

A twofold order parameter introduced in Ref. [13] was used as a quantitative measure of the existing degree of order in simulated systems,

$$g_2 \equiv \left\langle \frac{1}{N} \sum_{\langle R, R' \rangle} \delta_{s_R, -s_{R'}} e^{2i\theta_{R,R'}} \right\rangle, \qquad (20)$$

where $N$ is the number of spins, $\delta_{s_R, -s_{R'}}$ picks out pairs of spins at an interface, and $\theta_{R,R'}$ is the angle that a vector
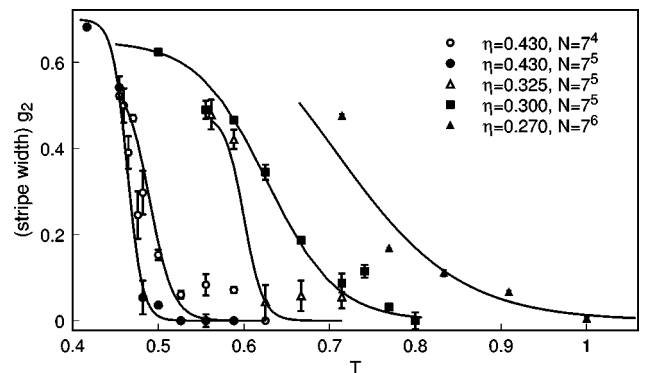


FIG. 8. The twofold order parameter $g_2$ is plotted as a function of temperature $T$ for several values of $\eta \equiv A/J$. With decreasing repulsion strength, stripes widen and the stripe melting temperature shifts upward. The solid lines are drawn as a guide to the eye. In the plot, $g_2$ is multiplied by the low-temperature value of the stripe width for each $\eta$, so all the curves approach unity at low temperature and are on the same scale.
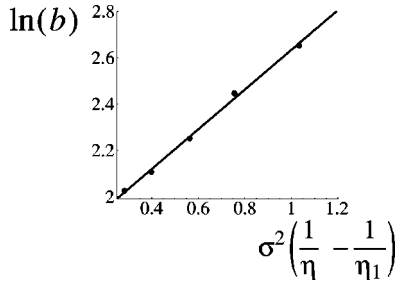
FIG. 9. Fit of stripe width simulation data, measured by the scaling parameter $b$, to Eq. (21).



FIG. 10. Fit of simulation data for the stripe melting temperature $T_m$ to Eq. (23).

joining sites $R$ and $R'$ makes with a reference direction. $g_2 = (1/\text{stripe width})$ for a system of perfectly straight stripes, and $g_2 = 0$ for systems in which no stripe order exists. $T_m$ was determined tracking $g_2$ as a function of temperature, shown in Fig. 8, each time checking for convergence with system size, except for the largest systems of $7^6 = 117\,649$ spins. Our method of extracting the order parameter $g_2$ from simulation data is discussed in detail in Appendix B. Figure 8 shows a trend of increasing $T_m$ with decreasing $\eta$, which is in excellent agreement with our analytic scaling theory [3].

Our scaling theory [3] matches points on a phase diagram parametrized by $J$, $A$, and $h$ to other points that exhibit the same pattern morphologies (i.e., stripes, bubbles, or intermediately shaped domains), only scaled by a factor $b$. It predicts how the domain length scale $b$ depends on the relative repulsion strength $\eta$ [3],

$$\ln b = \Gamma \sigma^2 \left( \frac{1}{\eta} - \frac{1}{\eta_1} \right). \tag{21}$$

In the above expression, $\Gamma$ is the surface tension of the domains, $\sigma$ is the area per spin ($\sqrt{3}/2$ for the triangular lattice, recalling that distances are measured in units of the lattice nearest neighbor distance so $\sigma$ is dimensionless), and $\eta_1$ is the value of $\eta$ at which $b$ is assigned to be 1. In the stripe phase, $b$ is measured by the stripe width,

$$b = \frac{(\text{average stripe width at } \eta)}{(\text{average stripe width at } \eta_1)}. \tag{22}$$

Equation (21) is valid when magnetization fluctuations within domains can be neglected and the surface tension $\Gamma$ is essentially constant. We observed that magnetization fluctuations within domains were extremely rare and took advantage of this fact to omit attempted Monte Carlo moves in the interior of domains, as described in Sec. II B. We would have preferred to access smaller values of $\eta$ where intradomain fluctuations are significant at the stripe melting temperature. This would have allowed us to test a phenomenological extension of the scaling theory [3] applicable to regions where $\Gamma$ and the average magnetization within domains vary with temperature. Unfortunately, domains become so large in this interesting case that simulations are not feasible.

According to Eq. (21), a plot of $\ln b$ vs $\sigma^2(\eta^{-1} - \eta_1^{-1})$ should yield a straight line whose slope is $\Gamma$. This is done for the stripe phase at zero field in Fig. 9. The excellent match to
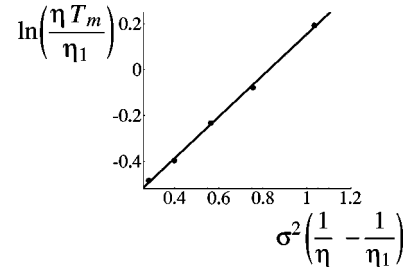
a linear relation confirms that $\Gamma$ is constant for the range of $\eta$ probed here. The value of $\Gamma$ extracted from the fit, $0.86 \pm 0.03$, is somewhat less than the zero-temperature limit of the surface tension, $\Gamma = 1$ ($T \to 0$). As temperature increases, $\Gamma$ should decrease from 1 at $T = 0$ to 0 at the point where domain structure is destroyed by fluctuations.

The scaling theory [3] also predicts how the zero-field stripe melting temperature depends on $\eta$,

$$\ln \left( \frac{\eta}{\eta_1} T_m \right) = \ln T_{m,1} + \Gamma \sigma^2 \left( \frac{1}{\eta} - \frac{1}{\eta_1} \right). \tag{23}$$

A plot of $\ln(\eta T_m / \eta_1)$ against $\sigma^2(\eta^{-1} - \eta_1^{-1})$ should yield another straight line with slope $\Gamma$. This is done in Fig. 10, and the extracted slope is $0.90 \pm 0.02$, in agreement with the domain length relation of Fig. 9 within statistical error.

In order to identify the nature of the phase transition leading to loss of twofold order in the studied systems, a plot of the dimensionless heat capacity per particle $C_v / Nk_B \equiv (1/N) \partial \langle E \rangle / \partial (k_B T) = (N)^{-1} (k_B T)^{-2} \langle (E - \langle E \rangle)^2 \rangle$ as a function of $(T - T_m)$ was generated and is shown in Fig. 11. There is no singularity in the behavior of $C_v$ for temperatures near $T_m$ at any value of $\eta$. The values of $C_v$ near stripe melting for $\eta = 0.270$, 0.300, and 0.325 are all quite close to each other, as would be expected if our scaling hypothesis were valid. The heat capacity for the largest value of
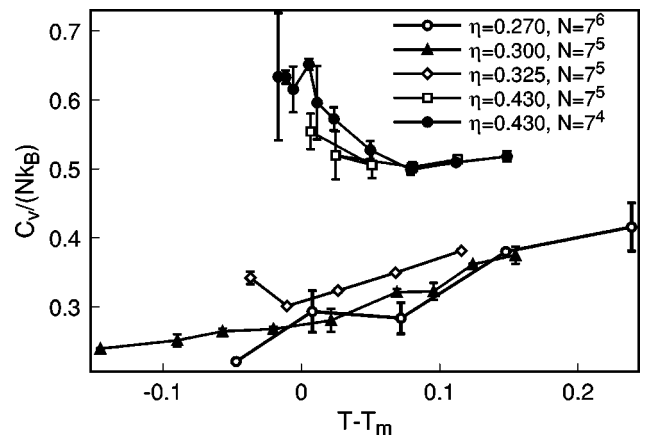


FIG. 11. The dimensionless heat capacity per particle, $C_V / Nk_B$, is shown as a function of temperature difference from the stripe melting temperature for several values of $\eta \equiv A/J$. In agreement with the Kosterlitz-Thouless mechanism, there is no heat capacity anomaly at the transition temperature ($T - T_m = 0$ in these plots).

$\eta$ (0.43), which corresponds to the thinnest stripes, does not lie close to the others, although no heat capacity singularity is observed here either. This ''anomalous'' case is likely the result of the stripes not being thick enough (i.e., large enough stripe width, compared to the lattice spacing) for the continuum approximation used to derive the scaling theory to hold.

The results for the heat capacity, together with the visual evidence of Figs. 7(a) and 7(b), are consistent with stripe melting mediated by topological defect unbinding, as discussed by KT theory. However, the scaling theory of Ref. [3] predicts that the possibility exists for an Isinglike disordering due to overturned spins to supplant the KT type stripe melting at very low $\eta$. These low values of the relative repulsion strength have proven to be inaccessible to our simulations. Equation (21) shows that the domain length grows faster than exponentially with $\eta^{-1}$. Approximately $10^7$ spins would be needed to simulate a system at the value of $\eta$ where, according to Eq. (23), the stripe melting temperature approaches the critical temperature of the bare Ising model.

Finite-size scaling analysis, which has been done for other systems [54–56], could have provided yet another piece of evidence for a KT type phase transition in the studied systems. Our attempt at collecting sufficient data for it proved to be computationally infeasible, due to the large number of particles per topological defect.

### B. Simulations in external fields

Hurley and Singer have previously observed that an external field causes a transition from the stripe phase to a bubble phase, both at zero [11] and finite [13] temperature. In simulations [13], the field at which twofold stripe order is lost decreases with increasing temperature, permitting the construction of a tentative phase diagram at the value of $\eta$ for which simulations were performed. Unlike mean-field predictions [32,37], the stripe phase in the presence of an external field gives way at elevated temperature to an isotropic phase of elongated bubbles, and not to an ordered lattice of bubbles. (The elongated bubble phase is not truly isotropic since the bubbles tend to align along preferred lattice directions.) At still higher field values the bubbles loose their elongation and approach a faceted polygonal ordered bubble lattice.

Our previous simulations [13] were performed for a particular value of $\eta$ that produced domains that were compatible with the system size we were capable of simulating at the time. The FMM and non-Metropolis sampling introduced in this work greatly extend the range of system sizes and $\eta$ values accessible to numerical investigation. We have studied systems with relative repulsion strengths $\eta$ spanning the range 0.27 to 0.43. For each $\eta$, temperatures corresponding to the ordered and melted stripe phases in zero field were chosen. At each of these temperatures, the system was equilibrated in gradually increasing external fields. Typical snapshots from simulations showing elongated bubbles and bubbles are shown in Figs. 7(c) and 7(d). At sufficiently high fields, a uniform spin-up (or, equivalently, spin-down) phase is reached. Magnetization as a function of external field from
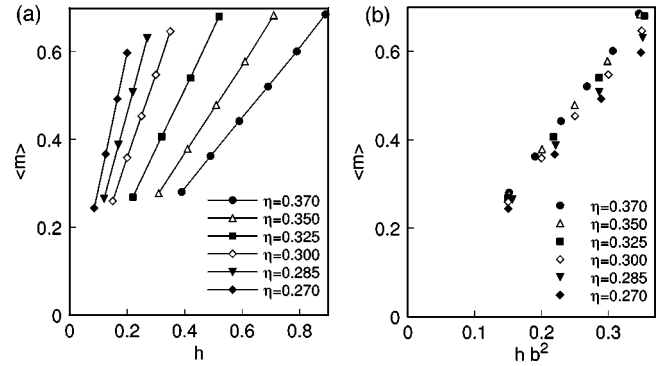


FIG. 12. Average magnetization per spin vs external magnetic field (a) and average magnetization per spin vs scaled external magnetic field (b) for a range of $\eta$ values.

our simulations is shown in Fig. 12(a). The corresponding states scaling theory we have derived [3] predicts that, for a system scaled by a factor $b$ from a reference system at $b = 1$, the field $h$ required to observe the same domain morphology as the reference system is

$$h = b^{-2} h_1, \tag{24}$$

where $h_1$ is the field value in the reference system. At points in parameter space for which $\eta$ is related to $\eta_1$ by Eq. (21), the temperature $T$ is related to that of the reference system $T_1$ by

$$\ln\left(\frac{\eta}{\eta_1} T\right) = \ln T_1 + \Gamma \sigma^2 \left(\frac{1}{\eta} - \frac{1}{\eta_1}\right) \tag{25}$$

[Eq. (23) is just Eq. (25) applied to a system at the point where stripes disorder], and $h = b^{-2} h_1$ will exhibit the same domain configurations apart from the change of scale. Properties such as the magnetization are not affected by the change in length scale. Scaled systems with the same value of $b^2 h$ should, according to Eq. (24), have the same magnetization as the reference system with field $h_1$. This prediction is tested in Fig. 12(b) and is seen to hold remarkably well. When plotted against $b^2 h$, the data of Fig. 12(a) collapse onto a single curve. Note that the temperature for each value of $\eta$ was chosen according to Eq. (25).

### IV. DISCUSSION

Numerical simulations of the Ising model with long-range repulsions can access only a limited range of system parameters. However, they provide valuable insights regarding the phase diagram of the model. The significance of computer simulations increases further having in mind that, to date, analytic theory treatments have not been able to describe all aspects of the rich phase behavior supported by the model. The purpose of this work is twofold. We test our analytic scaling theory [3] against computer simulation results and thereby establish the phase behavior of the dipolar Ising model within the scaling theory's range of validity. We also establish the mechanism of stripe melting in the range of parameters accessible to simulations.

The simplest version of our scaling theory [3] is valid only when domain boundaries in the system are sharp. This is also the only region of the phase diagram probed by simulations so far. As demonstrated in this work [Figs. 9 and 10], there is quantitative agreement between numerical data and analytic predictions concerning the stripe melting temperature as a function of the relative repulsion strength $\eta$ and magnetization as a function of external field $h$. The stripe phase region of the phase diagram is now firmly established to extend higher in temperature and contract with respect to $h$ as $\eta$ decreases.

A phenomenological extension to the scaling theory [3] predicts that magnetization/density fluctuations curb the increase in $T_m$ with decreasing relative repulsion strength. They also hinder stripe growth with increasing temperature at constant $\eta$. Unfortunately, observation of these effects is not accessible to simulations at present, due to the large system sizes $[O(10^7)$ particles] needed to probe the phase diagram regions in question.

For the values of the relative repulsion strength that are accessible to simulation ($\eta = 0.27$ to $0.43$), we observe [Figs. 7(a) and 7(b)] that the loss of twofold order in these systems is mediated by thermally induced defects in the stripe structure. The process occurs without any significant local magnetization/density fluctuations. The appearance of disclinations above $T_m$ and the absence of a heat capacity anomaly at the melting temperature point to a KT defect unbinding mechanism, although further evidence in the form of order parameter scaling [54–56] would be valuable. Unfortunately, extensive simulations up to our largest system (117 649 spins) could not provide the desired scaling information, indicating that numerical investigations of even larger systems are needed.

Another point of significance concerns our choice of a triangular underlying lattice. In many experimental systems, like Langmuir monolayers, stripes have continuous overall rotational symmetry (e.g., Ref. [22]). Magnetic films have an underlying lattice, but the anisotropy is often small, as one might conclude based on visual evidence from experimental observations (e.g., Ref. [9]). Therefore, models with continuous, isotropic orientational degrees of freedom, such as the planar $XY$ model, are appropriate for describing topological defect unbinding in these systems. Unlike the experimental systems or models such as the $XY$ model, stripes in the dipolar Ising model prefer to be aligned along certain lattice directions. This may be viewed as an additional symmetry breaking field that spoils the rotational invariance of the spin model. The symmetry breaking field is fourfold for a square lattice and sixfold for a triangular lattice.

The effect of symmetry breaking fields has been investigated [57] for the Villain model [58], which is closely related to the planar $XY$ model. An exact duality relation for the Villain model shows that a $p$-fold symmetry-breaking field is always a relevant perturbation at high temperatures. At low temperatures, in particular, in the vicinity of the KT phase transition (occurring at $T_{KT}$), the relevance of the symmetry-breaking field depends on $p$. For $p = 4$ (square lattice), the spin lattice becomes a relevant perturbation below the KT transition. For $p = 6$ (triangular lattice), however, it does not

become a relevant perturbation until $T > T_{KT}$. In order to make our results more applicable to continuum systems, we chose to work on a triangular ($p = 6$), rather than a square ($p = 4$) lattice. The work of Kashuba and Pokrovsky [59,60] and Abanov *et al.* [61] explores the effect of a fourfold anisotropy on the stripe phase. Our choice of a triangular lattice could explain the discrepancy of our heat capacity data with results obtained for a dipolar Ising model on a square lattice [39] according to which $C_v$ peaks at the melting phase transition. As discussed above, we find no $C_v$ anomalies near the defect-unbinding temperature. The difference in the observed heat capacity behavior could also be due to the very small system sizes of Ref. [39].

While our work settles several important issues regarding the mechanism through which stripe order is lost in the dipolar Ising model, new questions arise concerning regions of the phase diagram corresponding to $\eta \rightarrow 0$. Our scaling theory predicts that as the relative repulsion strength is decreased, the stripe melting temperature will rise toward the critical temperature of the bare Ising model $T_c$. If the stripe width happens to diverge less rapidly than the correlation length as $T_m \rightarrow T_c$, it would be possible to observe a crossover from defect unbinding to Isinglike spin disordering within stripes for very small values of $\eta$. Even though this region of the phase diagram was not amenable to simulations, we present a qualitative discussion illustrating that a single model could support both types of disordering mechanisms.

Consider a coarse-grained version of a system of stripes described by the Hamiltonian

$$-\frac{\mathcal{H}}{k_B T} = K_2 \sum_{\langle R, R'\rangle} \sigma_R \sigma_{R'} \vec{u}_R \cdot \vec{u}_{R'} + K_1 \sum_{\langle R, R'\rangle} \sigma_R \sigma_{R'} . \tag{26}$$

We interpret the $\sigma_R$ as coarse-grained variables measuring the degree of uniformity of spins within the stripes of the dipolar Ising model near $R$. A region of perfectly homogeneous stripe domains, containing an alternating series of $s_R = 1$ and $s_R = -1$ stripes, would be represented by either $\sigma_R = 1$ everywhere in that region, or $\sigma_R = -1$ everywhere. Hence the $\sigma_R$ are not directly interpretable as block averages of the $s_R$. The $\vec{u}_R$ are interpreted as vectors along the averaged normal to the stripe interfaces for coarse-grained blocks of stripes centered at $R$, and $K_1$ and $K_2$ are dimensionless coupling constants proportional to $1/T$. The coupling constant $K_1$ reflects how ordered the spins are within the stripes. Large $K_1$ implies almost no overturned spins within the stripes. The effective coupling between the stripe orientation variables $\vec{u}_R$ and $\vec{u}_{R'}$ is controlled by the coupling constant $K_2$ and by the alignment of the spin variables $\sigma_R$ and $\sigma_{R'}$. The correlation function $G(R,R') = \langle \sigma_R \sigma_{R'} e^{2i(\Theta_R - \Theta_{R'})} \rangle$, where $\Theta_R$ is the angle between $\vec{u}_R$ and a reference direction, measures the long-range stripe order. Long-range order may be destroyed either by topological defects in the stripes, in which case the average of the $e^{2i(\Theta_R - \Theta_{R'})}$ component
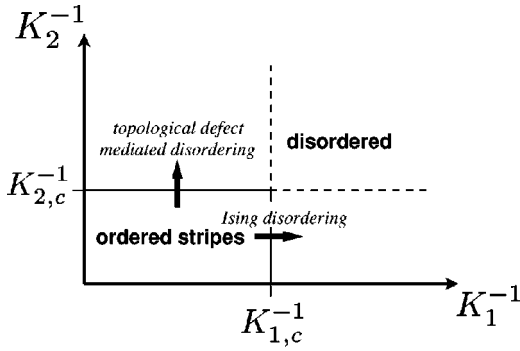
FIG. 13. Phase diagram for a qualitative model that supports both the defect unbinding and Isinglike disordering mechanisms.

switches from algebraic to exponential decay, or by Isinglike spin fluctuations which make the average of $\sigma_R \sigma_{R'}$ vanish at large separation.

The partition function for this model is given by

$$Z(K_1, K_2) = \text{Tr}_{\{\sigma_R, \vec{u}_R\}} \exp\left( K_2 \sum_{\langle R, R' \rangle} \sigma_R \sigma_{R'} \vec{u}_R \cdot \vec{u}_{R'} \right.$$
$$\left. + K_1 \sum_{\langle R, R' \rangle} \sigma_R \sigma_{R'} \right). \quad (27)$$

After the substitution $\vec{u}_R' = \sigma_R \vec{u}_R$, the partition function factors into an Ising-model part and an $XY$-model part,

$$Z(K_1, K_2) = \text{Tr}_{\{\sigma_R\}} \left[ e^{K_1 \sum_{\langle R, R' \rangle} \sigma_R \sigma_{R'}} \right] \text{Tr}_{\{\vec{u}_R'\}} \left[ e^{K_2 \sum_{\langle R, R' \rangle} \vec{u}_R' \cdot \vec{u}_{R'}'} \right]$$
$$= Z_{Ising}(K_1) Z_{XY}(K_2). \quad (28)$$

When $K_1$ and $K_2$ are both larger than their critical values $K_{1,c}$ and $K_{2,c}$, a system of coarse-grained blocks of ordered stripes with sharp interfaces is observed (Fig. 13). If $K_2$ is maintained larger than $K_{2,c}$, the system loses orientational order in an Isinglike manner as $K_1$ falls below $K_{1,c}$. In the opposite case of $K_1 > K_{1,c}$, the system loses orientational order in a KT type phase transition when $K_2$ falls below $K_{2,c}$.

The $\vec{u}_R$ degrees of freedom are disordered, as measured by $G(R, R')$, except at high $K_1$ *and* $K_2$. In this trivially solved model, the system may leave the ordered region via an Isinglike disordering of the $\sigma_R$ variables, or a KT disordering of the $\vec{u}_R' = \sigma_R \vec{u}_R$, which are effectively the same as the $\vec{u}_R$ when the $\sigma_R$ variables are strongly aligned. The dipolar Ising model may also have two mechanisms by which it can lose twofold stripe order, a defect-mediated transition at large $\eta$ and an Isinglike disordering at small $\eta$. This is suggested by the phenomenological extension of our scaling theory to small $\eta$ [3]. However, further analytical and numerical work is needed to confirm the crossover of the melting mechanism.

A systematic investigation of the relation between melting temperature and relative repulsion strength [Eq. (23)] that

would test our predictions awaits experimental realization. We have previously suggested [2,3] that compression-induced melting observed in Langmuir monolayers provides indirect confirmation of the inverse correlation between $T_m$ and $\eta$. We have argued that compression leads to an effective increase in $\eta$, causing $T_m$ to fall, thereby moving the system into a disordered region of the phase diagram. This argument is bolstered by the experimental observation that upon compression, stripes become thinner [22], as would be predicted for an increase in $\eta$ by the scaling relation of Eq. (21). More direct evidence for the inverse relation between $T_m$ and $\eta$ would be welcome.

Another feature of the dipolar Ising model and its lattice gas equivalent, which we believe would be amenable to experimental observation is a search for the crossover region between defect unbinding and Isinglike disordering of the stripe phase. Tracking the number of topological defects in the system, the magnetization/density in the stripe phase, or the heat capacity could corroborate, which disordering mechanism is in effect. In order to identify the crossover itself, a system with a "tunable" relative repulsion strength $\eta$ would be needed. Tuning $\eta$ could be achieved in different ways, depending on the experimental system. In the case of Langmuir monolayers, varying pH or adding co-surfactants could bring the desired effect. Variable $\eta$ values in thin magnetic films could be induced by changing the properties of the magnetic material.

## APPENDIX A: PROOF OF DETAILED BALANCE

Consider the microcanonical transition probability $\bar{W}(CD|C'D')$ from (system, demon) state $(C', D')$ to state $(C, D)$. As discussed in Sec. II B, the transition is allowed only if the demon energy $E_{D'}$ is greater than the difference in system energies $E_C - E_{C'}$. The microcanonical probability is, therefore, a step function

$$\bar{W}(CD|C'D') = \Theta(E_{C'} + E_{D'} - E_C). \quad (A1)$$

To compute the overall transition rate $W(C|C')$ from state $C'$ to state $C$, integrate $\bar{W}(CD|C'D')$ over all possible demon energies in the initial system state $C'$

$$W(C|C') = \int_0^\infty dE_{D'} \bar{W}(CD|C'D') \mathcal{P}(E_{D'}), \quad (A2)$$

where $\mathcal{P}(E_D) = \beta e^{-\beta E_D}$ is a normalized Boltzmann distribution function. Now consider the ratio of forward to reverse moves,

$$\frac{W(C|C')}{W(C'|C)} = \frac{\int_0^\infty dE_{D'}\Theta(E_{C'}+E_{D'}-E_C)\beta e^{-\beta E_{D'}}}{\int_0^\infty dE_D\Theta(E_C+E_D-E_{C'})\beta e^{-\beta E_D}}.$$

(A3)

Since the integral in the numerator (denominator) in the above equation evaluates to 1, if $E_{C'} \geq E_C (E_C \geq E_{C'})$, and to $e^{-\beta(E_C - E_{C'})}$, if $E_C \geq E_{C'}$ $(e^{-\beta(E_{C'} - E_C)},$ if $E_{C'} \geq E_C)$, the ratio of canonical transition probabilities becomes

$$\frac{W(C|C')}{W(C'|C)} = \frac{e^{-\beta E_C}}{e^{-\beta E_{C'}}}.$$

(A4)

Therefore, detailed balance is satisfied.

## APPENDIX B: STATISTICAL ANALYSIS OF SIMULATION DATA

The magnitude of the order parameter $g_2 \equiv \langle \hat{g}_2 \rangle = \langle (1/N)\Sigma_{\langle R,R'\rangle}\delta_{s_R,-s_{R'}}e^{2i\theta_{R,R'}}\rangle$ measures the degree of twofold orientational order, which is an indicator of the stripe phase. There is a technical problem associated with accumulating $g_2$. Since the orientation of the stripes is arbitrary, exhaustive averaging of the quantity $\hat{g}_2$ in a finite system will eventually drive the average to zero after all stripe orientations are sampled. This is a generic problem associated with accumulating an order parameter in the absence of a symmetry breaking field. Alternatively, one might generate the average of $|\hat{g}_2|$, which would be immune to trivial vanishing of the order parameter via rotational invariance. However, the positive definite quantity $|\hat{g}_2|$ yields a nonvanishing average proportional to $N^{-1/2}$ in the disordered phase.

We avoid the undesirable features of the averages $\langle \hat{g}_2 \rangle$ and $\langle |\hat{g}_2| \rangle$ by analyzing the distribution of $\hat{g}_2$ in the complex plane. In the ordered phase, the distribution peaks at $|\hat{g}_2| > 0$ [Fig. 14(a)], while in the disordered phase the distribution is centered around $|\hat{g}_2| = 0$ [Fig. 14(b)]. The order parameter values shown in Fig. 8 are extracted from simulations by fitting the distribution to an analytic ansatz described below.

Since the underlying triangular lattice introduces a three-
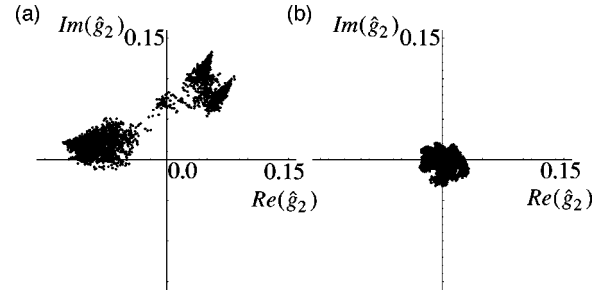


FIG. 14. Sample distributions of the order parameter $g_2$ in the complex plane for (a) ordered stripes and (b) melted stripes.

fold symmetry breaking field leading to three preferred stripe orientations in the system, we find that the probability density of $\hat{g}_2$ peaks at three locations, separated by $2\pi/3$, lying at angles $\theta = \pi$ and $\pm \pi/3$ with respect to the abscissa in the complex plane. (These preferred stripe orientations are equivalent to $\theta = 0, \pi/3$, and $2\pi/3$. The angle assignment is a matter of convention.) Even though the stripe orientation tends to fall along these three directions, the system is still susceptible to averaging $\langle \hat{g}_2 \rangle$ to zero when more than one of the three preferred directions are sampled, as frequently occurs in the computer simulations [Fig. 14(a)].

We estimated the degree of orientational order by fitting the radial distribution of $\hat{g}_2$ data from each simulation to a Gaussian form using a probability distribution function of the form

$$\mathcal{P}(|\hat{g}_2|) = \int d\hat{\phi} P(\hat{g}_2) \propto |\hat{g}_2| e^{-(1/2\sigma^2)(|\hat{g}_2| - \langle \hat{g}_2 \rangle)^2}, \quad (B1)$$

where $\hat{\phi}$ is the phase angle of $\hat{g}_2$. The value of $\langle \hat{g}_2 \rangle$ obtained by a nonlinear least squares fit of Eq. (B1) to numerical data is what is reported in Fig. 8. In some cases, $|\hat{g}_2|$ exhibited bimodal behavior, as the system made infrequent crossings between ordered and disordered configurations. To analyze the order parameter for these simulations, we used the sum of two weighted Gaussians for the radial distribution function, one of which was centered around the origin: $P(|\hat{g}_2|) = (1-\alpha)e^{-(1/2\sigma_0^2)|\hat{g}_2|^2} + \alpha e^{-(1/2\sigma^2)(|\hat{g}_2| - \langle \hat{g}_0 \rangle)^2}$. The parameter $\alpha$ was optimized during the fitting and $\alpha \langle \hat{g}_2 \rangle$ is reported in Fig. 8.

[1] M. Seul and D. Andelman, Science **267**, 476 (1995).
[2] A. D. Stoycheva and S. J. Singer, Phys. Rev. Lett. **84**, 4657 (2000).
[3] A. D. Stoycheva and S. J. Singer, Phys. Rev. E **64**, 016118 (2001).
[4] C. Kittel, Phys. Rev. **70**, 965 (1946).
[5] C. Kooy and U. Enz, Philips Res. Rep. **15**, 2 (1960).
[6] A. A. Thiele, J. Appl. Phys. **41**, 1139 (1970).
[7] R. E. Rosensweig, M. Zahn, and R. Shumovich, J. Magn. Magn. Mater. **39**, 127 (1983).
[8] W. A. Barker and G. A. Gehring, J. Phys. C **16**, 6415 (1983).

[9] M. Seul and R. Wolfe, Phys. Rev. A **46**, 7519 (1992).
[10] H. M. McConnell, Mol. Cryst. Liq. Cryst. **176**, 321 (1989).
[11] M. M. Hurley and S. J. Singer, J. Phys. Chem. **96**, 1938 (1992).
[12] M. M. Hurley and S. J. Singer, J. Phys. Chem. **96**, 1951 (1992).
[13] M. M. Hurley and S. J. Singer, Phys. Rev. B **46**, 5783 (1992).
[14] K.-O. Ng and D. Vanderbilt, Phys. Rev. B **52**, 2177 (1995).
[15] R. M. Weis and H. M. McConnell, Nature (London) **310**, 47 (1984).
[16] R. M. Weis and H. M. McConnell, J. Phys. Chem. **89**, 4453

(1985).

[17] W. M. Heckl and H. Möhwald, Ber. Bunsenges. Phys. Chem. **90**, 1159 (1986).

[18] M. Lösche and H. Möhwald, J. Colloid Interface Sci. **131**, 56 (1989).

[19] H. Möhwald, Thin Solid Films **159**, 1 (1988).

[20] H. M. McConnell, Annu. Rev. Phys. Chem. **42**, 171 (1991).

[21] M. Seul and M. J. Sammon, Phys. Rev. Lett. **64**, 1903 (1990).

[22] M. Seul and V. S. Chen, Phys. Rev. Lett. **70**, 1658 (1993).

[23] K. Kern, H. Niehus, A. Schatz, P. Zeppenfeld, J. Goerge, and G. Comsa, Phys. Rev. Lett. **67**, 855 (1991).

[24] J. H. Weaver, Nav. Res. Rev. **XLIII**, 16 (1991).

[25] H. Hörnis, J. R. West, E. H. Conrad, and E. Ellialtioğlu, Phys. Rev. B **47**, 13 055 (1993).

[26] S. Müller, P. Bayer, C. Reischl, K. Heinz, B. Feldmann, H. Zillgen, and M. Wuttig, Phys. Rev. Lett. **74**, 765 (1995).

[27] P. Bak, D. Mukamel, J. Villain, and K. Wentowska, Phys. Rev. B **19**, 1610 (1979).

[28] P. Bak and D. Mukamel, Phys. Rev. B **19**, 1604 (1979).

[29] V. I. Marchenko, JETP Lett. **55**, 73 (1992).

[30] D. Vanderbilt, Surf. Rev. Lett. **4**, 811 (1997).

[31] S. Leibler and D. Andelman, J. Phys. (Paris) **48**, 2013 (1987).

[32] D. Andelman, F. Broçhard, and J.-F. Joanny, J. Chem. Phys. **86**, 3673 (1987).

[33] O. L. Alerhand, D. Vanderbilt, R. D. Meade, and J. D. Joannopoulos, Phys. Rev. Lett. **61**, 1973 (1988).

[34] D. Vanderbilt, O. L. Alerhand, R. D. Meade, and J. D. Joannopoulos, J. Vac. Sci. Technol. B **7**, 1013 (1989).

[35] S. A. Brazovskiĭ, Sov. Phys. JETP **41**, 85 (1975).

[36] J. Toner and D. R. Nelson, Phys. Rev. B **23**, 316 (1981).

[37] T. Garel and S. Doniach, Phys. Rev. B **26**, 325 (1982).

[38] I. Booth, A. B. MacIsaac, J. P. Whitehead, and K. De'Bell, Phys. Rev. Lett. **75**, 950 (1995).

[39] J. Arlett, J. P. Whitehead, A. B. MacIsaac, and K. De'Bell, Phys. Rev. B **54**, 3394 (1996).

[40] L. Greengard and V. Rokhlin, J. Comp. Physiol. **73**, 325 (1987).

[41] M. Creutz, Phys. Rev. Lett. **50**, 1411 (1983).

[42] M. Creutz, Phys. Rev. Lett. **69**, 1002 (1992).

[43] C. Sagui and T. A. Darden, Annu. Rev. Biophys. Biomol. Struct. **28**, 155 (1999).

[44] F. Zhao, MIT Technical Report 996, 1987 (unpublished).

[45] J.-S. Wang and R. H. Swendsen, Physica A **167**, 565 (1990).

[46] R. H. Swendsen, Comput. Phys. Commun. **65**, 281 (1991).

[47] R. H. Swendsen, J.-S. Wang, and A. M. Fernberg, Top. Appl. Phys. **71**, 75 (1995).

[48] R. H. Swendsen and J.-S. Wang, Phys. Rev. Lett. **58**, 86 (1987).

[49] U. Wolff, Phys. Rev. Lett. **62**, 361 (1989).

[50] J.-S. Wang, R. H. Swendsen, and R. Kotecký, Phys. Rev. B **42**, 2465 (1990).

[51] L. Onsager, Phys. Rev. **65**, 117 (1944).

[52] R. J. Baxter, *Exactly Solved Models in Statistical Mechanics* (Academic Press, New York, 1982).

[53] Animations of our simulations of an Ising model with additional dipolar repulsions can be viewed at http://chemistry.ohio-state.edu/~singer/DipolarIsingSimulations.

[54] D. Frenkel and R. Eppenga, Phys. Rev. A **31**, 1776 (1985).

[55] A. Alavi, Phys. Rev. Lett. **64**, 2289 (1990).

[56] A. Alavi, Mol. Phys. **71**, 1173 (1990).

[57] J. V. José, L. P. Kadanoff, S. Kirkpatrick, and D. R. Nelson, Phys. Rev. B **16**, 1217 (1977).

[58] J. Villain, J. Phys. (Paris) **36**, 581 (1975).

[59] A. Kashuba and V. L. Pokrovsky, Phys. Rev. Lett. **70**, 3155 (1993).

[60] A. B. Kashuba and V. L. Pokrovsky, Phys. Rev. B **48**, 10 335 (1993).

[61] A. Abanov, V. Kalatsky, V. L. Pokrovsky, and W. M. Saslow, Phys. Rev. B **51**, 1023 (1995).